Chinese Chemical Letters 37 (2026) 111126

Contents lists available at ScienceDirect

Chinese Chemical Letters

journal homepage: www.elsevier.com/locate/cclet

Ba-doping to modulate surface electronic states in $Eu_{0.9}Ba_{0.1}O_x$ catalysts for oxidation coupling of methane

Shibo Zhang[a,b], Xiang Chu[a,b], Meng Zhao[a,*], Baokang Geng[a,b], Xiao Wang[a,b,*], Shuyan Song[a,b,*], Hongjie Zhang[a,b,c,*]

[a] State Key Laboratory of Rare Earth Resource Utilization, Changchun Institute of Applied Chemistry, Chinese Academy of Sciences, Changchun 130022, China
[b] School of Applied Chemistry and Engineering, University of Science and Technology of China, Hefei 230026, China
[c] Department of Chemistry, Tsinghua University, Beijing 100084, China

ARTICLE INFO

Article history:
Received 11 January 2025
Revised 14 March 2025
Accepted 20 March 2025
Available online 20 March 2025

Keywords:
Oxidative coupling of methane
Spray pyrolysis
Ba-doping
Oxygen vacancies
Europium oxide

ABSTRACT

The oxidative coupling reaction of methane (OCM) process offers a promising pathway for the direct conversion of methane into high value C_2 hydrocarbons (C_2H_6 and C_2H_4), albeit facing the challenges of harsh reaction conditions and competing overoxidation reaction. Herein, Ba-doped Eu_2O_3 synthesized *via* the spray pyrolysis method was employed as highly active dopant catalyst for the methane oxidative coupling reaction. The prepared $Eu_{0.9}Ba_{0.1}O_x$ catalyst showed satisfactory reactivity and stability, with a C_{2+} product selectivity of 52.4%, a C_{2+} yield of 16.2%, and a stabilization time of at least 100 h. The incorporation of Ba atoms into Eu_2O_3 lattice leads to an increased molar ratio of Eu^{2+}/Eu^{3+} and a higher oxygen vacancies (O_v) concentration. Such modulation of surface electronic state significantly improves the adsorption and activation behavior of oxygen, thereby accelerating the production of reactive oxygen species (O_2^-). Meanwhile, the acid-base properties of Eu_2O_3 substrate also undergo obvious alteration with more basic site generation after Ba doping, which is conducive to the stabilization activated oxygen. O_2^- substances can promote the activation of methane into methyl radicals, and also facilitate the dehydrogenation of ethane into ethylene, thus improving the catalytic activity.

© 2026 Published by Elsevier B.V. on behalf of Chinese Chemical Society and Institute of Materia Medica, Chinese Academy of Medical Sciences.

Methane, the main component of shale gas and natural gas, holds immense potential for the single step production of value added hydrocarbons and oxygenated compounds owing to its abundant availability [1–4]. However, it is hard to directly activate or convert methane due to its chemical internes including the low polarizability, negligible electron affinity and high C–H bond dissociation energy [5,6]. Therefore, high temperature is usually required to overcome the thermodynamic barriers and initiate reaction [7–9]. Among various direct transformation methods, the OCM reaction has garnered research interest in the past decades because it can produce valuable C_{2+} hydrocarbons [10]. The OCM is believed to require the following processes: (1) The C–H bond in methane dissociates to give methyl radicals, catalyzed by the surface active oxygen; (2) The coupling reaction involving the obtained methyl radical result in the formation of ethane; (3) The dehydrogenation process converts ethane into ethylene [11]. Simultaneously, methane may also undergo deep dehydrogenation and oxidation, resulting in the formation of carbon dioxide and carbon monoxide, which poses a major obstacle to achieving high yields of C_2 hydrocarbons during the OCM process, rendering it a formidable challenge [12]. Therefore, it is imperative to search for well-crafted catalysts that can optimize the adsorption/desorption behavior of intermediates and effectively attain high yields of the desired products.

Rare-earth (RE) oxide with unfilled 4f orbitals and the high thermal stability, have been a hot research topic in OCM reactions [13–16]. However, despite their potential, the selectivity and yield of C_2 product over RE oxide catalysts remain suboptimal. To address this issue, surface modification and regulation of the catalysts represent a promising strategy [17]. In the OCM reaction, oxygen vacancies play a crucial role in activating oxygen to produce reactive oxygen species. These species, in turn, facilitate the subsequent dehydrogenation steps of methane and ethane [18]. Many efforts have been made to increase the amount of oxygen vacancies on the catalysts surface [19]. For instance, Sim *et al.* successfully doped Al into La_2O_3 lattice, which promoted the formation of oxygen vacancies and consequently increased the C_2 selectivity from 35% to 42% [20]. Zhang *et al.* combined La and Ce to form a

* Corresponding authors.
E-mail addresses: zhaomeng@ciac.ac.cn (M. Zhao), wangxiao@ciac.ac.cn (X. Wang), songsy@ciac.ac.cn (S. Song), hongjie@ciac.ac.cn (H. Zhang).

https://doi.org/10.1016/j.cclet.2025.111126
1001-8417/© 2026 Published by Elsevier B.V. on behalf of Chinese Chemical Society and Institute of Materia Medica, Chinese Academy of Medical Sciences.

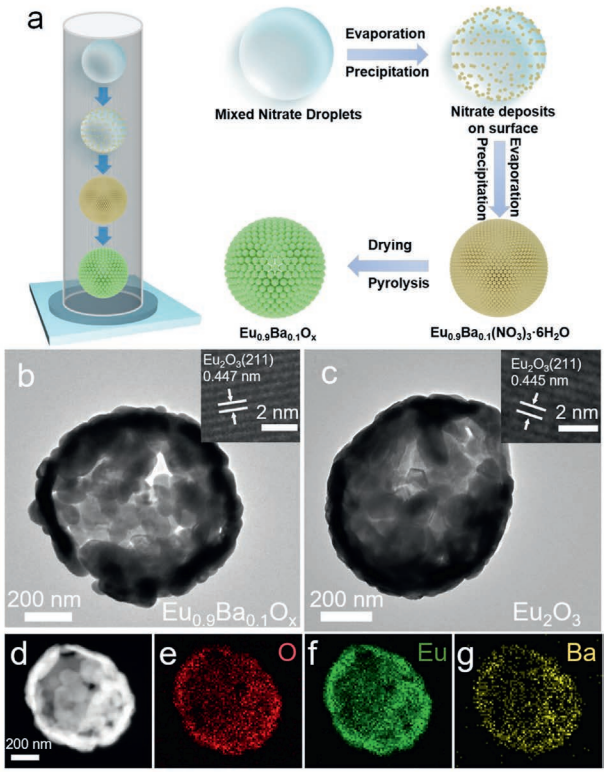


Fig. 1. Structure of the $Eu_{0.9}Ba_{0.1}O_x$ catalyst. (a) Schematic diagram of catalyst synthesis (b, c) TEM image and HRTEM image of $Eu_{0.9}Ba_{0.1}O_x$ and Eu_2O_3 (d-g) Corresponding EDX mapping images of $Eu_{0.9}Ba_{0.1}O_x$.

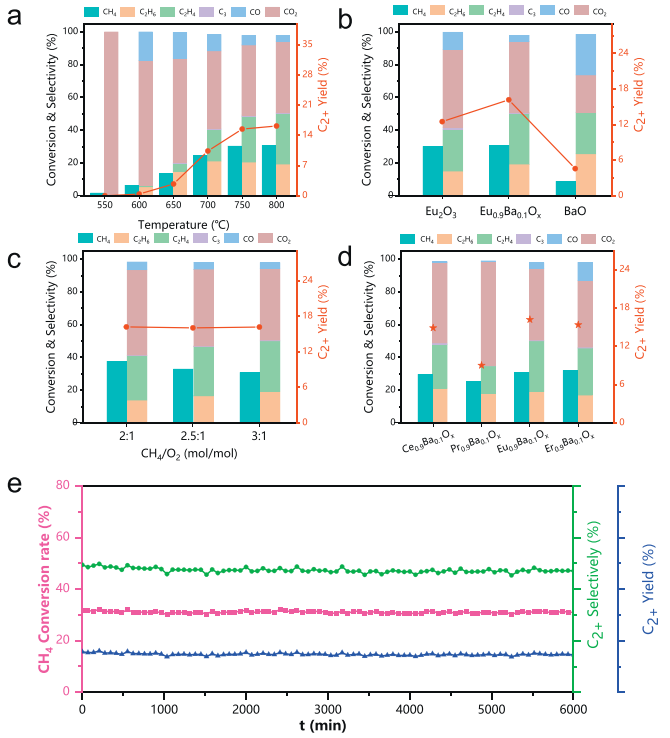


Fig. 2. Catalytic performance investigations. (a) Temperature effect for $Eu_{0.9}Ba_{0.1}O_x$. (b) Catalytic performances of Eu_2O_3, $Eu_{0.9}Ba_{0.1}O_x$ and BaO. (c) CH_4/O_2 (mol/mol) ratios of the $Eu_{0.9}Ba_{0.1}O_x$ catalyst. (d) Redox OCM performance comparison of $Ce_{0.9}Ba_{0.1}O_x$, $Pr_{0.9}Ba_{0.1}O_x$, $Eu_{0.9}Ba_{0.1}O_x$ and $Er_{0.9}Ba_{0.1}O_x$. (e) Long-term stability test of the $Eu_{0.9}Ba_{0.1}O_x$ catalyst at 800 °C, 3:1 CH_4/O_2 ratio, and 2000 mL h^{-1} g_{cat}^{-1} GHSV for 6000 min.

stable $La_2Ce_2O_7$ compound with a disordered defective cubic fluorite structure and increased C_2 yield from 12 % to 15 % [21]. It is therefore clearly evident that there is still a great deal of room for improvement in terms of C_2 selectivity and conversion rates in OCM. Hence, the strategic design of the material surface, coupled with the augmentation of oxygen vacancies, emerges as promising strategies for optimizing the performance of OCM reactions.

In this study, Ba-doped Eu_2O_3 catalysts were prepared using ultrasonic spray pyrolysis, exhibiting high C_2 selectivity and high stability for OCM reactions. A variety of characterization techniques were employed to gain insight into the structural and physicochemical properties of the Ba-doped catalysts, including transmission electron microscopy (TEM), X-ray diffraction (XRD) analysis, X-ray photoelectron spectroscopy (XPS), electron paramagnetic resonance (EPR) and programmed temperature rise desorption (TPD) analysis. The findings demonstrate that Ba doping in Eu_2O_3 can markedly enhance the number of basic sites and the concentration of oxygen vacancies on the catalyst surface. This results in the generation of reactive oxygen species, which in turn improves the C_2 selectivity and thus enhances the catalytic performance.

As illustrated in Fig. 1a, Ba-doped Eu_2O_3 catalyst was prepared *via* ultrasonic spray pyrolysis. The spray solution was initially underwent ultrasonic treatment within a spray generator, and followed by calcining in a tube furnace, wherein the aerosol precursor decomposed into powder [22]. The SEM and TEM images displays that the obtained products are regular spherical polyhedron with a diameter of 0.5–3 μm (Fig. S1 in Supporting information and Figs. 1b and c). The sharp contrast observed between the center and the edges allows for the inference that the primary grains possess a hollow structure. The creation of the unique hollow structure can be attributed to the rapid evaporation of water from the droplet surface within the tube furnace, which is accompanied by the swift deposition of nitrate onto the particle surfaces, leading to the formation of $M(NO_3)_3$–$6H_2O$ shells. Once the solvent evaporation is complete, the nitrate undergoes dehydration and ultimately decomposes, yielding single shell hollow oxide particles [23]. Throughout the entire process, the spray droplets can serve as individual reactors. The high-resolution TEM image in the inset demonstrates that the crystal region of pure Eu_2O_3 exhibits a lattice stripe spacing of 0.445 nm, which corresponds to the (211) planar spacing of cubic Eu_2O_3. In contrast, the lattice fringe spacing of the Ba-doped Eu_2O_3 crystal region is 0.447 nm, which can be attributed to the substitution of Ba^{2+} for Eu^{3+} along with a bigger ionic radius of Ba (135 pm) than that of Eu (95 pm). Further characterization by the corresponding EDX elemental mapping reveals the uniform distribution of Eu, Ba, and O elements (Figs. 1d-g). The X-ray diffraction (XRD) pattern of Eu_2O_3 (Fig. S2 in Supporting information) is in accordance with the standard card (PDF #34–0392) and exhibits a space group of $Ia\bar{3}$ [24,25]. No diffraction peaks belong to Ba species were detected, and the position of the (222) crystal facet diffraction peak shifted from 28.5° (for Eu_2O_3) to 28.4° (for $Eu_{0.9}Ba_{0.1}O_x$), thereby confirming the successful incorporation of Ba into the Eu_2O_3 lattice.

As shown in Fig. 2, we evaluated the OCM catalytic performance of various catalysts. As shown in Fig. 2a, while the reaction temperature rises from 550 °C to 800 °C, both the methane conversion and C_{2+} selectivity exhibit a steady augmentation. That is account for the fact that higher temperatures facilitate the cleavage of the C–H bond within the methane molecule. Specifically, the methane conversion of $Eu_{0.9}Ba_{0.1}O_x$ catalyst was 30.9 % as the temperature reached 800 °C. Among all the products, the selectivity for ethane and ethylene were 19.2 % and 30.9 % respectively, while there was a minor proportion of C_3 products and a significant majority of by-products consisting of CO_2. As a contrast, the methane conver-

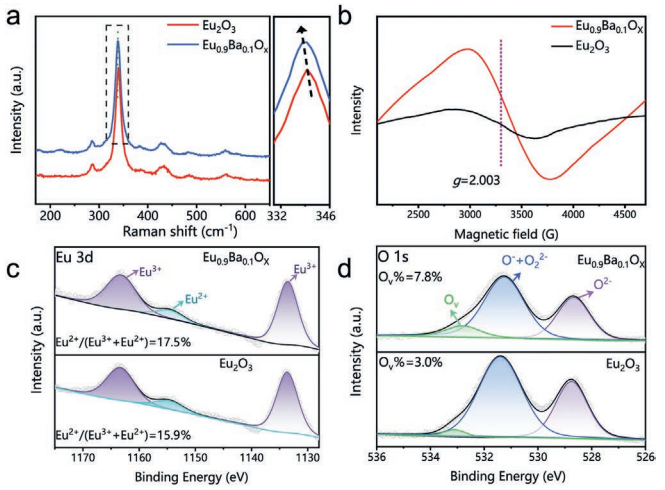


Fig. 3. Characterizations of catalyst structure. (a) Raman spectra of $Eu_{0.9}Ba_{0.1}O_x$ and Eu_2O_3. (b) EPR spectra of $Eu_{0.9}Ba_{0.1}O_x$ and Eu_2O_3. (c) Eu 3d and (d) O 1s XPS spectra of $Eu_{0.9}Ba_{0.1}O_x$ and Eu_2O_3.

sion over bare Eu_2O_3 was 30.1 %, but the C_{2+} selectivity was relatively low at 41.6 %. The C_{2+} selectivity of bare BaO was comparable to that of $Eu_{0.9}Ba_{0.1}O_x$, however, the methane conversion was significantly lower, standing at just 8.7 % (Fig. 2b, Figs. S3 and S4 in Supporting information). The results underscore the superiority of Ba-doping in terms of enhancing the selectivity of C_{2+}. To ascertain the role of oxygen, we conduct further investigation into the performance of OCM reaction under O_2-lean and O_2-rich conditions. As shown in Fig. 2c, as the feeding ratio of CH_4 to O_2 was increased from 2:1 to 3:1, the methane conversion continued to decrease from 37.8 % to 30.9 %, but the C_{2+} selectivity continued to increase from 42.9 % to 50.2 %. The reason for this phenomenon is that an O_2-rich environment favors not only the activation of methane but also the undesirable overoxidation of methane, leading to a simultaneous increase in methane conversion and a decrease in C_{2+} selectivity, and a similar situation occurs with the reduction of GHSV (Fig. S5 in Supporting information) [15]. Subsequently, an investigation was extended to encompass other rare earth elements beyond Eu, as exemplified in Fig. 2d. In a comparative analysis, the catalytic activity exhibited by $Eu_{0.9}Ba_{0.1}O_x$ surpasses that of $Ce_{0.9}Ba_{0.1}O_x$, $Pr_{0.9}Ba_{0.1}O_x$ and $Er_{0.9}Ba_{0.1}O_x$ catalysts (Figs. S6-S10 in Supporting information). The C_{2+} yields of the $Eu_{0.9}Ba_{0.1}O_x$ catalysts were superior to most of the catalysts reported in the literature (Fig. S11 in Supporting information).

Finally, the findings depicted in Fig. 2e illustrate that the $Eu_{0.9}Ba_{0.1}O_x$ catalyst maintains a methane conversion rate within a narrow band of 31 %–32 % over a prolonged reaction period of 100 h. The catalyst exhibits high thermal stability and no carbon buildup (Fig. S12 in Supporting information). Concurrently, the yield of C_2 products remains consistently stable at approximately 15 %–16 %, exhibiting extremely stable OCM reaction activity. After undergoing rigorous durability testing, the samples were thoroughly characterized. As shown in Fig. S13 (Supporting information), the XRD pattern remained nearly indistinguishable from their initial state, with no impurity diffraction peaks detected. TEM analysis provided additional confirmation that the morphology and structural integrity of the catalysts sustained unchanged throughout the entire testing period (Fig. S14 in Supporting information).

Fig. 3a and Fig. S15 (Supporting information) illustrate the Raman spectra of pure Eu_2O_3 and $Eu_{0.9}Ba_{0.1}O_x$, which were acquired under ambient conditions utilizing a 633 nm excitation laser. Both samples exhibit a prominent band at 339.5 cm^{-1}, along with two distinct peaks at 285.8 and 432.2 cm^{-1}. The band centered at 339.5 and 432.2 cm^{-1} are assigned to the F_g mode of Eu_2O_3 crystal, whereas the band at 285.8 cm^{-1} is ascribed to the combined $F_g + E_g$ mode [26]. In the $Eu_{0.9}Ba_{0.1}O_x$ sample, the aforementioned peaks exhibit a slight shift towards lower wavelengths, which can be attributed to the phonon confinement effects arising from an increased O_v concentration [27]. To gain better qualitative and quantitative insights into the unpaired electrons in substances, EPR measurement was constructed. As shown in Fig. 3b, the g-value signal associated with unpaired electrons captured by oxygen vacancies (2.003) displays a noticeable augmentation in the $Eu_{0.9}Ba_{0.1}O_x$ catalyst [28]. The presence of O_v facilitates the dissociative adsorption of O_2 to generate surface-active electrophilic oxygen, which is a pivotal active site for OCM reactions [29]. All of the aforementioned results powerful confirm that the incorporation of Ba atoms into Eu_2O_3 lattice plays an instrumental role in enhancing the concentration of oxygen vacancies and enabling efficient oxygen activation.

We further investigate the surface elemental composition and fine chemical state of the Eu_2O_3 catalyst both before and after doping Ba by XPS analysis [30]. In the Eu 3d spectra (Fig. 3c), it can be found that the peak at 1133.6 and 1163.3 eV corresponds to Eu^{3+} and the peak at 1154.6 eV is attributed to Eu^{2+} [31]. By calculating the areas under the Eu^{3+} and Eu^{2+} peaks, it was determined that the percentage of the Eu^{2+} state in the $Eu_{0.9}Ba_{0.1}O_x$ catalyst increased from 15.9 % to 17.5 % after Ba doping. The concentration of oxygen vacancies in the catalyst is closely related to the percentage of the Eu^{2+} state. In order to maintain charge conservation, a decrease in the Eu valence state leads to the appearance of oxygen vacancies. As shown in Fig. 3d, the O 1s spectrum in $Eu_{0.9}Ba_{0.1}O_x$ catalyst can be deconvoluted into three secondary peaks, which have been assigned to the oxygen vacancies O_v (532.8 eV), surface-adsorbed oxygen O_2^{2-} and O^- (529.8 eV) and lattice oxygen O^{2-} (528.8 eV) [32]. It is noteworthy that the substantial rise in O_v content, from 3.0 % in Eu_2O_3 to 7.8 % in $Eu_{0.9}Ba_{0.1}O_x$, coincides with the increased in Eu^{2+} content on the catalyst surface. The proportion of Eu^{2+} and O_v in the $Eu_{0.9}Ba_{0.1}O_x$ catalyst is almost constant before and after the reaction (Figs. S16 and S17 in Supporting information). The above results further confirm that the incorporation of Ba atoms into Eu_2O_3 lattice can effectively promote the formation of oxygen vacancies, as evidenced by both Raman and EPR analyses. It is also demonstrated that the quantity of O_v is the key to promote the OCM catalytic performance.

For better understanding the structure-activity relationship of catalysts, the O_2-TPD characterization was utilized to get a deeper insight into the intrinsic correlation between surface oxygen species and catalytic performance. As shown in Fig. 4a, the O_2-TPD profile was divided into three sections: the desorption peaks of surface physically adsorbed oxygen (50–300 °C), surface chemisorbed oxygen (300–550 °C), and surface lattice oxygen species (550–800 °C) [33]. It has been proven that the presence of surface chemisorbed oxygen facilitates the activation of methane and enhance the subsequent dehydrogenation of ethane whereas the surface lattice oxygen (O^{2-}) promotes the complete oxidation of hydrocarbons to CO_x. As expected, it can be observed that the two catalysts exhibit distinct desorption profiles for oxygen species. Specifically, the amount of desorbed chemisorbed oxygen was higher in the $Eu_{0.9}Ba_{0.1}O_x$ catalyst compared to Eu_2O_3, aligning with our findings regarding their respective catalytic performances. In H_2-TPR curve (Fig. S18 in Supporting information), the $Eu_{0.9}Ba_{0.1}O_x$ catalysts have stronger and more pronounced reduction peaks compared to the Eu_2O_3 catalysts, indicating that the oxygen on the surface of the $Eu_{0.9}Ba_{0.1}O_x$ catalysts is more likely to bind with hydrogen and form oxygen vacancies.

It is well known that the acidity and alkalinity of the catalyst surface are significant variables which significantly influence the efficacy of the OCM process. On the one hand, the conversion of

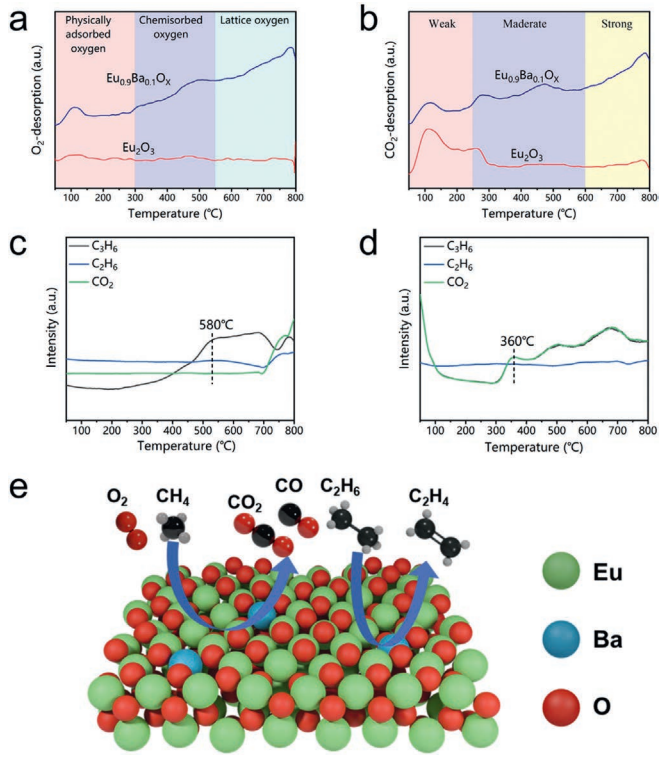


Fig. 4. Mechanism investigation. (a) CO_2-TPD of $Eu_{0.9}Ba_{0.1}O_x$ and Eu_2O_3. (b) O_2-TPD of $Eu_{0.9}Ba_{0.1}O_x$ and Eu_2O_3. (c) CH_4-TPSR spectra of $Eu_{0.9}Ba_{0.1}O_x$ catalysts pretreated with He at 700 °C. (d) CH_4-TPSR spectra of $Eu_{0.9}Ba_{0.1}O_x$ catalysts without He pretreatment. (e) Structural schematic diagram of $Eu_{0.9}Ba_{0.1}O_x$.

oxygen into reactive oxygen species on the catalyst surface necessitates a specific alkalinity. On the other hand, the generated reactive oxygen species also requires a certain alkalinity to be stabilized [34]. Accordingly, the alkaline sites on the catalyst surface were investigated through CO_2-TPD (Fig. 4b). The alkaline sites were classified into three categories based on the CO_2 desorption temperature, namely weakly alkaline sites at 50–250 °C, moderately strong alkaline sites at 250–600 °C, and strongly alkaline sites at 600–800 °C [35]. However, weakly basic sites are prone to be inactive at elevated temperatures, while strongly basic sites are susceptible to inactivation due to the formation of carbonates upon combining with CO_2; thus, medium-strength basic sites are optimal for achieving high C_2 selectivity. It can be found that the number of medium-strength basic sites of the Ba-doped $Eu_{0.9}Ba_{0.1}O_x$ catalyst increased significantly in comparison with that of Eu_2O_3, which is consistent with the observed catalytic activity.

In order to identify whether CH_4 is activated to methyl radicals by lattice oxygen of metal oxides or surface reactive oxygen species in this catalytic system, we performed CH_4-TPSR experiments. Prior to test, the $Eu_{0.9}Ba_{0.1}O_x$ catalyst was first purged with He at 700 °C to remove reactive oxygen species (O_2^-, O^-, *etc.*) on the catalyst surface. The results are shown in Fig. 4c, where the coupling product of the OCM reaction (C_3H_6), was rapidly formed at 580 °C, and the deep oxidation product (CO_x), appeared at 750 °C. This indicates that the coupling reaction starts to occur above 580 °C. To verify the possibility of the reactive oxygen species mechanism, the $Eu_{0.9}Ba_{0.1}O_x$ catalyst was directly subjected to CH_4-TPSR experiments. As shown in Fig. 4d, the product peaks of C_3H_6 and CO_2 can be detected at a low temperature of 360 °C. The above comparative results intuitively indicate that reactive oxygen species play an important role in the activity of $Eu_{0.9}Ba_{0.1}O_x$ catalysts, which is because the coupling reaction reacts violently at 360 °C in the presence of reactive oxygen species, and the rapid coupling reaction temperature rises to 580 °C after removal of the reactive oxygen species.

Based on the comprehensive analysis of the above characterization results, the catalytic pathway for OCM reaction over the $Eu_{0.9}Ba_{0.1}O_x$ catalyst is clearly illustrated in Fig. 4e. The doping of Ba ions significantly increased the number of oxygen vacancies on the catalyst surface, thereby effectively facilitated the adsorption and activation of O_2. This, in turn, fostered the evolution of O_2^- species and further promoted the dissociative coupling of methane to form ethane. Additionally, the presence of O_2^- species also facilitated the dehydrogenation of ethane to ethylene, ultimately enhancing the overall performance of the oxidative coupling of methane (OCM) reaction.

In conclusion, a monolayer hollow $Eu_{0.9}Ba_{0.1}O_x$ catalyst was successfully prepared and utilized for the OCM reaction. The doping of Ba ions in cubic Eu_2O_3 promoted the formation of O_v and increased the number of active oxygen sites. The $Eu_{0.9}Ba_{0.1}O_x$ catalyst exhibited satisfactory performance and stability in the OCM reaction, achieving a CH_4 conversion of 30.9 %, a selectivity of 52.4 % and a yield of 16.2 % for C_{2+} product, and maintained its catalytic activity for up to 100 h. The Ba doping of Eu_2O_3 increased the number of surface oxygen vacancies, which is conducive to the activation of oxygen into active O_2^-, and increased the number of medium-strength basic sites on the surface, which is conducive to the stabilization of the generated reactive oxygen species. This strategy holds great promise for advancing the design of highly active and stable rare earth oxide-based materials for catalytic applications.

Declaration of competing interest

The authors declare that they have no known competing financial interests or personal relationships that could have appeared to influence the work reported in this paper.

CRediT authorship contribution statement

Shibo Zhang: Writing – original draft, Investigation, Formal analysis. **Xiang Chu:** Investigation. **Meng Zhao:** Writing – review & editing, Formal analysis. **Baokang Geng:** Investigation. **Xiao Wang:** Writing – review & editing, Supervision, Project administration. **Shuyan Song:** Writing – review & editing, Validation, Supervision, Project administration. **Hongjie Zhang:** Supervision.

Acknowledgments

This work was supported by the financial aid from National Science and Technology Major Project of China (No. 2023YFB3508000), National Natural Science Foundation of China (Nos. 22020102003, 22025506, 22271274 and U23A20140), Jilin Province Science and Technology Development Plan Project (Nos. 20230101035JC, 20230101022JC and 20240402056GH), Jilin Province Innovation and Entrepreneurship Talent Project (No. E31S6105) and Yunan Province Science and Technology Development Plan Project (No. 202301BC070001–003). X. Wang acknowledges funding from National Natural Science Foundation of China Outstanding Youth Science Foundation of China (Overseas).

Supplementary materials

Supplementary material associated with this article can be found, in the online version, at doi:10.1016/j.cclet.2025.111126.

References

[1] X. Sun, G. Liu, T. Shen, et al., Small 20 (2024) e2310857.
[2] M. Li, A.C. van Veen, Appl. Catal. B: Environ. 237 (2018) 641–648.

[3] S.R. Patlolla, K. Katsu, A. Sharafian, et al., Renew. Sust. Energ. Rev. 181 (2023) 113323.
[4] J. Kim, M. Ferree, S. Gunduz, et al., ChemCatChem 15 (2023) 122026.
[5] P. Wang, R. Shi, Y. Zhao, et al., Angew. Chem. Int. Ed. 62 (2023) e202304301.
[6] Y. Wang, G. Hong, Y. Zhang, et al., Angew. Chem. Int. Ed. 62 (2023) e202310525.
[7] A.L.A. Marinho, F.S. Toniolo, F.B. Noronha, et al., Appl. Catal. B: Environ. 281 (2021) 119459.
[8] A.L.A. Marinho, R.C. Rabelo-Neto, F. Epron, et al., Appl. Catal. B: Environ. 268 (2020) 118387.
[9] N. Sun, J. Zhang, L. Ling, et al., Fuel 354 (2023) 129398.
[10] J. Kim, Y.J. Kim, M. Ferree, et al., Appl. Catal. B: Environ. 321 (2023) 122026.
[11] A. Zanina, V.A. Kondratenko, H. Lund, et al., ACS Catal. 12 (2022) 15361–15372.
[12] C. Karakaya, R.J. Kee, Prog. Energy Combust. Sci. 55 (2016) 60–97.
[13] Y. Jiang, H. Fu, Z. Liang, et al., Chem. Soc. Rev. 53 (2024) 714–763.
[14] X. Wu, X. Wang, L. Zhang, et al., Angew. Chem. Int. Ed. 63 (2024) e202317594.
[15] K. Zhao, Y. Gao, X. Wang, et al., Nat. Commun. 14 (2023) 7749.
[16] J. Xu, Y. Zhang, X. Xu, et al., ACS Catal. 9 (2019) 4030–4045.
[17] K. Wang, M. Lv, T. Si, et al., J. Hazard. Mater. 461 (2024) 132479.
[18] Y. Gambo, A.A. Jalil, S. Triwahyono, et al., J. Ind. Eng. Chem. 59 (2018) 218–229.
[19] Y. Ivanova, R. Petrov, S. Reshetnikov, et al., Mater. Today Chem. 26 (2022) 101124.
[20] Y. Sim, J. Yoo, J.M. Ha, et al., J. Energy Chem. 35 (2019) 1–8.
[21] Z. Zhang, Y. Gong, J. Xu, et al., Catal. Today 400-401 (2022) 73–81.
[22] H. Du, K. Huang, M. Li, et al., Nano Res. 11 (2018) 1490–1499.
[23] J. Leng, Z. Wang, J. Wang, et al., Chem. Soc. Rev. 48 (2019) 3015–3072.
[24] K. Yuan, Y.W. Zhang, Inorg. Chem. Front. 7 (2020) 4256–4280.
[25] M. Luo, M. Wang, W. Niu, et al., Chem. Eng. J. 412 (2021) 128471.
[26] M.V. Abrashev, N.D. Todorov, J. Appl. Phys. 116 (2014) 103508.
[27] J. Ibáñez, O. Blázquez, S. Hernández, et al., J. Raman Spectrosc. 49 (2018) 2021–2027.
[28] S.M. Wu, X.L. Liu, X.L. Lian, et al., Adv. Mater. 30 (2018) e1802173.
[29] R. Feng, P. Niu, B. Hou, et al., J. Energy Chem. 67 (2022) 342–353.
[30] C. Zheng, J. Feng, Z. Wei, et al., Chem. Eng. J. 467 (2023) 143390.
[31] M. Wang, P. Guo, Y. Zhang, et al., J. Hazard. Mater. 349 (2018) 224–233.
[32] Y. Zhu, X. Wu, Z. Wu, et al., Adv. Funct. Mater. 34 (2024) 2409324.
[33] T. Wu, Y. Wei, J. Xiong, et al., J. Energy Chem. 91 (2024) 331–344.
[34] T. Wu, P. Zhang, Y. Wei, et al., ACS Catal. 14 (2024) 1882–1902.
[35] R.S. Pal, S. Rana, S.K. Sharma, et al., Chem. Eng. J. 458 (2023) 141379.